Nanoscale

PAPER

View Article Online
View Journal | View Issue

Cite this: *Nanoscale*, 2025, **17**, 17579

Tunable resonant Raman scattering with temperature in vertically aligned 2H-SnS_2†

Atul G. Chakkar, *[a] Deepu Kumar, [a] Ashok Kumar,[b] Mahesh Kumar [b] and Pradeep Kumar *[a]

Received 27th April 2025,
Accepted 28th June 2025

DOI: 10.1039/d5nr01717c

rsc.li/nanoscale

Two-dimensional semiconducting materials have a wide range of applications in various fields due to their excellent properties and rich physics. Here, we report a detailed investigation of temperature-dependent Raman and photoluminescence measurements on vertically aligned 2H-SnS_2 grown by the CVD method. Our results established the tunability of resonant Raman scattering with varying temperature, *i.e.*, a crossover between resonance and non-resonance conditions for the current system. We also discussed the temperature as well as laser power dependence of the low-frequency asymmetric Raman mode, which is the interlayer shear mode. The temperature dependence of the intensity of the phonon modes also manifests the tunability of the resonant Raman scattering with temperature. Our temperature-dependent photoluminescence measurement shows the strong temperature dependence of the excitonic peaks and this is confirmed by the laser power dependence of the photoluminescence measurement at room temperature. Our investigation may help to design and fabricate devices based on vertically aligned 2H-SnS_2 and other similar materials in the future.

1. Introduction

Recently, two-dimensional (2D) layered semiconducting transition metal dichalcogenide materials have gained more research interest due to their unique properties, mainly large intrinsic band gap, and excitonic features and possible potential applications in gas sensing, optoelectronics, energy storage, and electronic devices.[1–3] Among the family of 2D materials, vertically aligned (VA) tin disulfide SnS_2 in the 2H phase has emerged as a potential candidate for chemical gas sensing, optoelectronics, photodetectors, and other device applications due to its large surface area-to-volume ratio, high transistor switching ratio, fast photodetection, high electrical conductivity, wide band gap, and excitonic feature.[4–8] Additionally, it is also cost-effective, low in toxicity, and has high stability. SnS_2 is a polar semiconductor with a band gap (E_g) of ~2.3–2.5 eV,[9] and hence it may provide a crucial path to study excitonic features.

In the resonant as well as non-resonant Raman scattering process, these excitonic energy states in semiconducting materials play a crucial role. The resonance conditions could be achieved by changing the incident excitation laser energy as well as by changing the temperature. In Group-6 TMD, the resonance phenomena in MoS_2 and WS_2 are well studied using Raman measurement as the function of laser excitation, temperature, and number of layers.[5,10–14] In the case of 2H-SnS_2, the resonance effect has been reported only as a function of laser excitation[15] and not as a function of temperature. Here, we performed a detailed temperature-dependent Raman and photoluminescence measurement to study the resonance effect in vertically aligned 2H-SnS_2. A study of the thermal properties of such potential semiconducting candidates explores more properties that may be helpful in various applications such as thermoelectric power generation and in device applications like transistors and sensors.[16,17] Thermodynamic properties such as thermal expansion, thermal conductivity, and specific heat are strongly affected by the anharmonicity effect and other underlying phenomena. Due to anharmonicity, the phonon has a finite lifetime and reduces self-energy. Anharmonicity strongly influences the thermal transport, and electronic and optoelectronic properties of materials. In layered 2D transition metal dichalcogenides (TMDs) and other materials, the electronic, optoelectronic, and thermal properties are associated with anharmonic effects and to understand the anharmonicity and phonon dynamics in such materials, a temperature-dependent Raman spectroscopy investigation is important.[18–28] Raman spectroscopy is one of the most promising non-destructive tools that can be used to investigate the thermal, structural, electrical, magnetic, and optical properties of 2D materials.[29–40]

In this work, we have performed detailed temperature-dependent Raman and photoluminescence (PL) measure-

[a]*School of Physical Sciences, Indian Institute of Technology Mandi, Mandi 175005, India. E-mail: atulchakkar16@gmail.com, pkumar@iitmandi.ac.in*
[b]*Department of Electrical Engineering, Indian Institute of Technology Jodhpur, Jodhpur, 342037, India*

† Electronic supplementary information (ESI) available. See DOI: https://doi.org/10.1039/d5nr01717c

ments in a temperature range of ~10–310 and 5–320 K, respectively, and analyzed them to investigate the dynamics of the phonon modes and the exciton, respectively, as a function of temperature. We also performed power-dependent Raman measurements in the low-frequency regime and power-dependent PL measurements with 325 nm laser excitation to investigate the excitonic nature of the observed PL peaks.

2. Experimental details

We performed the temperature-dependent Raman and PL measurements on vertically aligned (VA) 2H-SnS_2 flakes grown by the chemical vapor deposition (CVD) method.[41,42] Both Raman and PL measurements were conducted using a Horiba Lab-Ram HR Evolution Raman spectrometer in backscattering configuration, while the temperature was changed using a closed-cycle refrigerator (Montana cryostat) over a temperature range of ~5–320 K, with a temperature accuracy of ±0.1 K. For temperature-dependent Raman measurements, we used a laser excitation wavelength of 532 nm (2.33 eV), and kept very low laser power on sample, at ≤0.2 mW, to avoid local heating effects. We recorded the Raman spectrum using a 50× long working objective lens to focus incident light with a grating of 1800 groves per mm. We also performed power-dependent Raman measurements in the low-frequency regime. For PL measurements, we used a laser excitation wavelength of 325 nm (3.81 eV), and PL spectra were recorded using a 15× NUV objective lens to focus incident light on the sample with a grating of 600 groves per mm. We also performed power-dependent PL measurements at room temperature to investigate the excitonic nature of the observed PL peaks.

3. Results and discussion

3.1. Lattice vibrations in VA SnS_2

Bulk 2H-SnS_2 belongs to the point group D_{3d}^3 (space group $P\bar{3}m1$, #164), and has a hexagonal structure.[9,42] Bulk 2H-SnS_2 consists of 3 atoms per unit cell, which gives rise to nine phonon branches at the Γ-point of the Brillouin zone, expressed by following irreducible representation as $\Gamma_{\text{irred.}} = A_{1g} + 2A_{2u} + E_g + 2E_{2u}$.[9,15,43–45] There are 6 optical phonon branches, which are divided into three Raman-active ($A_{1g} + E_g$) and three infrared-active ($A_{2u} + E_u$) branches. The remaining three branches ($A_{2u} + E_u$) correspond to the acoustic phonons. The phonon modes with symmetry E are doubly degenerate and appear due to the in-plane vibration of atoms, while the phonon modes with symmetry A correspond to the non-degenerate out-of-plane vibrations of atoms. Fig. 1(a) shows the Raman spectrum of SnS_2 in a spectral range of 10–800 cm^{-1} recorded at 300 K. Insets in the yellow-shaded area are the

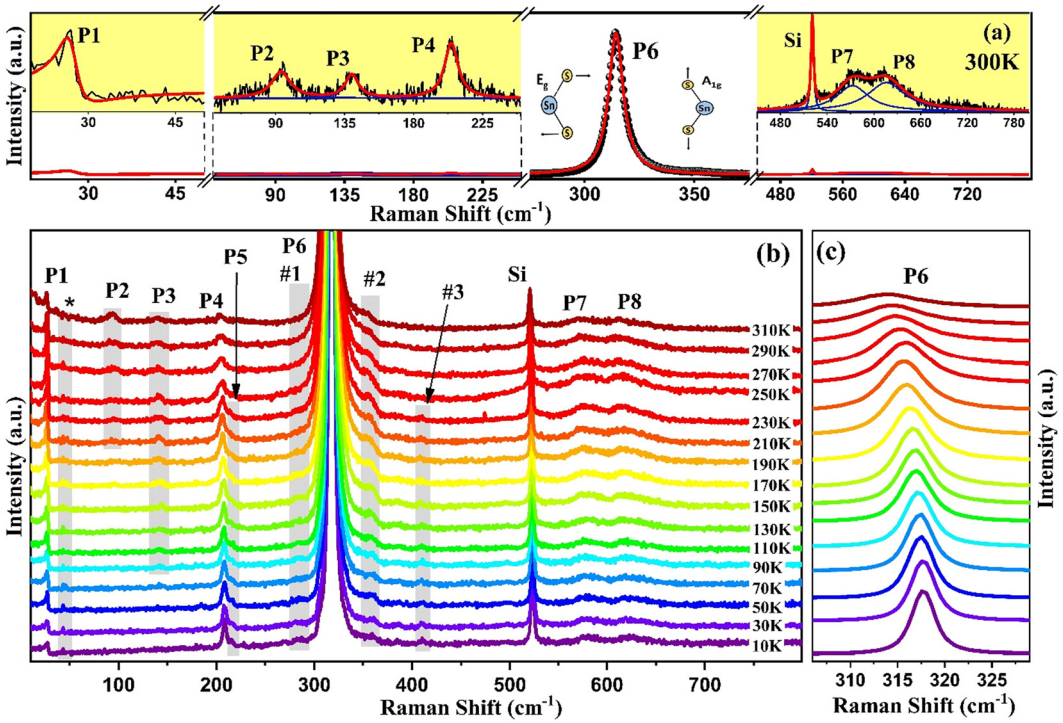

Fig. 1 (a) The Raman spectrum of VA SnS_2 in a spectral range of 10–800 cm^{-1} recorded at 300 K. Insets in the yellow shaded area are the amplified spectra in the spectral range of 10 to 50 cm^{-1}, 50 to 250 cm^{-1} and 450 to 800 cm^{-1}. One inset shows a ball-and-stick diagram representing the lattice vibration corresponding to the in-plane (E_g) and out-of-plane (A_{1g}) Raman active modes. (b) The temperature evolution of the Raman spectrum in the temperature range of ~10–310 K. (c) The temperature evolution of the most prominent phonon mode P6 in the temperature range of ~10–310 K.

amplified spectra for the spectral range of 10–50 cm^{-1}, 50–250 cm^{-1}, and 450–800 cm^{-1}. We have fitted the spectra using a sum of Lorentzian functions in order to extract phonon self-energy parameters, *i.e.*, mode frequency (ω), full width at half maximum (FWHM), and intensity of the individual modes. In the low-frequency regime, the peak P1 observed at ~27 cm^{-1} could be attributed to the interlayer shear/breathing mode, which appears due to the interaction between the adjacent layers. A very strong characteristic peak, P6, located at ~314 cm^{-1}, is attributed to the first-order Raman active A_{1g} mode and appears due to the out-of-plane vibration of S atoms in the opposite direction with fixed Sn atoms. A very weak peak, P4, located near ~205 cm^{-1}, is attributed to the first-order Raman active E_g mode and originates due to the in-plane vibration of both S and Sn atoms in the opposite direction. In addition to these characteristic Raman modes, we also observed a few additional modes from which some of the modes are intense at our highest recorded temperature while some of them are intense at low temperature. For example, the signal intensities for phonons P2 at ~94 cm^{-1} and P3 at ~140 cm^{-1} are observed to be strong at our highest recorded temperature (~310 K) while these signals vanished completely at very low temperatures. However, peak P5 at ~215 cm^{-1} is strong at low temperatures, and is absent at high temperatures, as shown in Fig. 1(b). Peaks P7 at ~580 cm^{-1} and P8 at ~624 cm^{-1} could be attributed to second-order phonons and are attributed to $E_u(TO) + A_{2u}(LO)$ and $2E_u(LO)$, respectively.[43] These two phonons are observed to be strong at high temperatures compared to their intensity at low temperatures. Furthermore, we also noticed a few extremely weak phonon peaks marked by asterisk (*) and number (#) symbols. The self-energy parameters of these modes could not be extracted using a Lorentzian fitting function due to their very weak nature. It is worth noting that the emergence/disappearance of phonon modes as a function of temperature may be an indication of the presence of a resonance effect. The modulation of this effect with temperature, which is a typical phenomenon in these kinds of semiconducting materials, will be discussed in more detail later.

3.2. Temperature dependence of the phonon modes

3.2.1. Phonon anharmonicity and thermal expansion coefficient. Fig. 2(a–d) shows the temperature dependence of the frequency (ω) and linewidth (FWHM) of the P3–P8 phonon modes in the temperature range of ~10–310 K. We observed that a phonon softening and broadening for all of the phonons occurred with increasing temperature with anomalous kinks/jumps near ~220–270 K in frequency/FWHM for some of the phonons. The changes in frequency of P4, P6, P7, and P8 are observed to be ~4.1, 3.3, 5.3 and 7.7 cm^{-1}, respectively. On the other hand, the changes in the FWHM of P4, P6, and P8 are found to be ~6.6, 5.4, and 5.6 cm^{-1}, respectively. Surprisingly, the change in the FWHM of the P7 mode is found to be significantly large (~57 cm^{-1}). It should be noted that in our recorded temperature range, the phonon modes generally soften or broaden by a value of 1–2 cm^{-1}. The observed large change in frequency and FWHM of the phonon modes may indicate the involvement of electron–phonon coup-

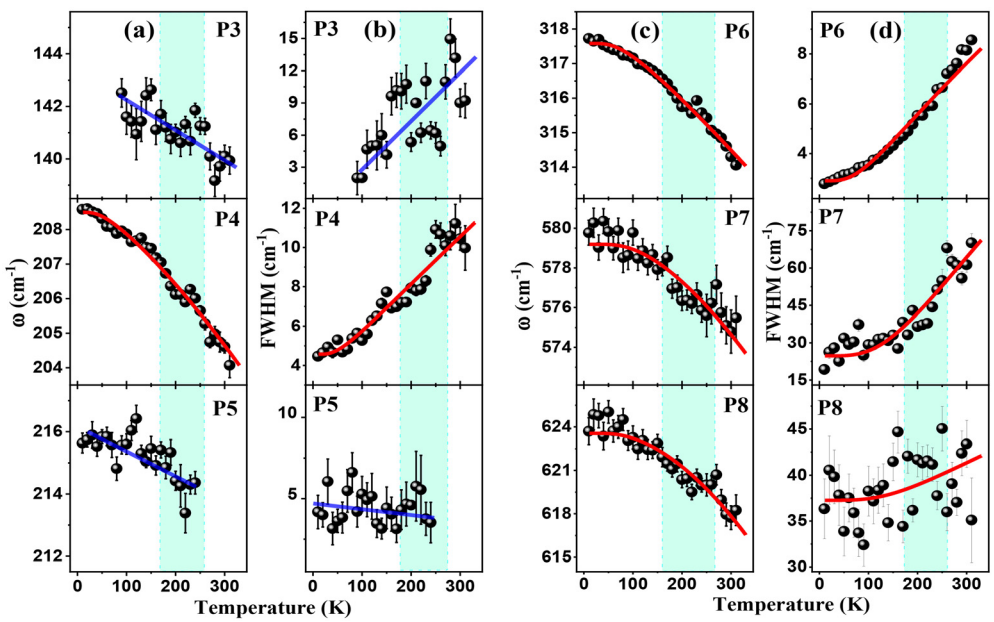

Fig. 2 (a) and (b) Temperature dependence of frequency and FWHM of the phonon modes P3–P5, respectively and (c) and (d) temperature dependence of the frequency and FWHM of the phonon modes P6–P8, respectively, for VA SnS_2. The solid red lines are the fitted curves as described in the text and the semi-transparent blue lines are guides for the eye. The error bars, which represent the standard error, were acquired by Lorentzian fitting in order to extract the self-energy parameters.

ling, which plays a crucial role in phonon self-energy parameters under resonance conditions. However, the reason for the extremely large change in the FWHM of the P7 mode is still not clear and may be the subject of future ongoing investigations. Nevertheless, P7 and P8 modes are second-order phonon modes.[43]

Generally, in 2D TMD materials, temperature-dependent frequency changes of phonons may be understood using the contribution of (i) the anharmonic effect and (ii) the thermal expansion of the lattice. The change in the frequency of the phonon modes as a function of temperature considering the above two effects may be given as:[46,47]

$$\Delta\omega(T) = \Delta\omega_{\text{anh.}}(T) + \Delta\omega_{\text{latt.}}(T) \quad (1)$$

The first term in eqn (1) corresponds to the change in the frequency of the phonon modes due to the anharmonic effect, which arises from the phonon–phonon interaction *via* three and four phonon processes and is given as:[48]

$$\Delta\omega_{\text{anh}}(T) = \omega(T) - \omega_0 = A\left(1 + \frac{2}{(e^x - 1)}\right) + B\left(1 + \frac{3}{(e^y - 1)} + \frac{3}{(e^y - 1)^2}\right) \quad (2)$$

where $x = \hbar\omega_0/2k_BT$ and $y = \hbar\omega_0/3k_BT$ are associated with the three- and four-phonon decay processes, respectively. Constants A and B are the self-energy fitting parameters associated with the three- and four-phonon anharmonic processes, respectively. Generally, the change in the linewidth of the phonon modes as a function of temperature can be understood by considering three- and four-phonon anharmonic effects and is given as:[48]

$$\Delta\Gamma(T) = \Gamma(T) - \Gamma(0) = C\left(1 + \frac{2}{(e^x - 1)}\right) + D\left(1 + \frac{3}{(e^y - 1)} + \frac{3}{(e^y - 1)^2}\right) \quad (3)$$

where the constants C and D are the self-energy fitting parameters, which show the strength of the phonon–phonon interaction associated with the three- and four-phonon anharmonic processes, respectively. In Fig. 2(a)–(d), the solid red lines are the fitted curves using eqn (2) and (3). The semi-transparent blue lines are drawn to act as a guide for the eye. The best extracted values of the self-energy fitting parameters are listed in Table 1.

The second term in eqn (1) corresponds to the change in frequency due to the thermal expansion of the lattice and is given as:

$$\Delta\omega_{\text{latt}}(T) = \omega_0\left\{\exp\left(-3\gamma\int_{T_0}^{T}\alpha(T)\mathrm{d}T - 1\right)\right\} \quad (4)$$

where γ is the Gruneisen parameter and $\alpha(T)$ is the linear thermal expansion coefficient (TEC) of the phonon modes. For convenience, the product of the phonon mode Gruneisen parameter and the TEC may be expressed by a polynomial of temperature and is given as:

$$\gamma\alpha(T) = a_0 + a_1T + a_2T^2 + \ldots \quad (5)$$

where a_0, a_1, and a_2 are the constant parameters and are obtained by fitting the frequency of the corresponding phonon modes using a combination of eqn (2) and (4) in the temperature range of 10–310 K. For the case of SnS_2, the value of the Gruneisen parameter (γ) of the phonon modes is unknown, hence for each phonon mode we have taken three different values, *i.e.*, γ = 1, 2, and 3. Fig. 3 shows the temperature dependence of the extracted thermal expansion coefficient ($\alpha(T)$) in the temperature range of ~10–310 K. For phonon modes P4 (A_{1g}) and P6 (A_{1g}), the TEC ($\alpha(T)$) increases with increasing temperature up to ~240 K and decreases with a further increase in the temperature. A positive value of the TEC indicates that the current system is expanding, and it also demonstrates the temperature dependence. Extraction of thermal expansion coefficients for 2D materials is helpful in strain engineering, heterostructure design, and nanodevice fabrication. In 2D materials, the study of thermal properties, such as the anharmonic effect, thermal expansion, *etc.*, are the most important because of the wide range of applications in the field of devices. A detailed investigation of such thermal properties may provide crucial understanding and may provide useful information for device fabrication and other applications.

3.2.2. Temperature-dependent intensity of the phonon modes. The temperature-dependent intensity of the phonon modes in 2D semiconducting materials may provide crucial information/understanding about their electronic and optical properties.[5,49–51] In this section, we focus on the temperature-dependent intensity of the phonons. Fig. 4(a) and (b) show the temperature-dependent intensity for some of the prominent phonon modes, *i.e.*, P4, P6 and P7, P8, respectively. The intensities of P4, P6, and P8 increase gradually with increasing temperature and attain maximum values at around 200–220 K. Interestingly, the intensity is observed to decrease with a

Table 1 List of self-energy fitting parameters corresponding to the phonon modes in VA 2H-SnS_2, fitted using the equation as described in the text. The unit is cm^{-1}

Mode assignment	ω_0	A	B	Γ_0	C	D
P4	209.5 ± 0.2	−0.9 ± 0.2	0.03 ± 0.02	2.9 ± 0.6	1.6 ± 0.8	0.06 ± 0.1
P6	319.3 ± 0.3	−1.7 ± 0.4	−0.02 ± 0.1	1.5 ± 0.1	1.2 ± 0.1	0.2 ± 0.1
P7	583.2 ± 0.3	−3.2 ± 0.0	−0.8 ± 0.1	15.0 ± 0.3	2.7 ± 0.3	7.0 ± 0.4
P8	626.1 ± 0.8	−0.6 ± 0.2	−2.0 ± 0.2	35.5 ± 0.2	1.0 ± 0.3	0.7 ± 0.3

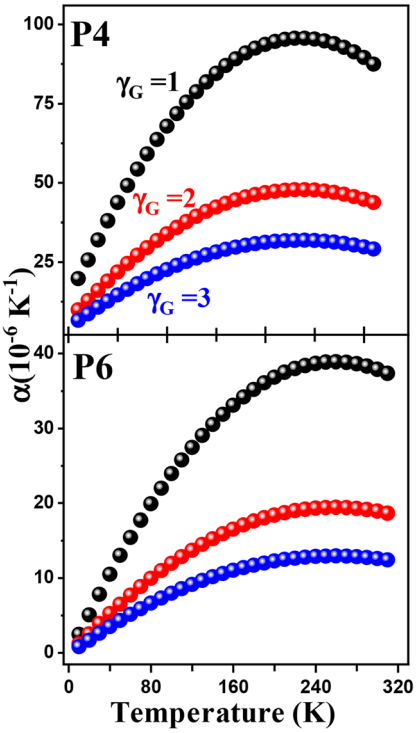

Fig. 3 The variation of the linear thermal expansion coefficient as a function of the temperature for peaks P4 and P6 in the temperature range of ~10–310 K.

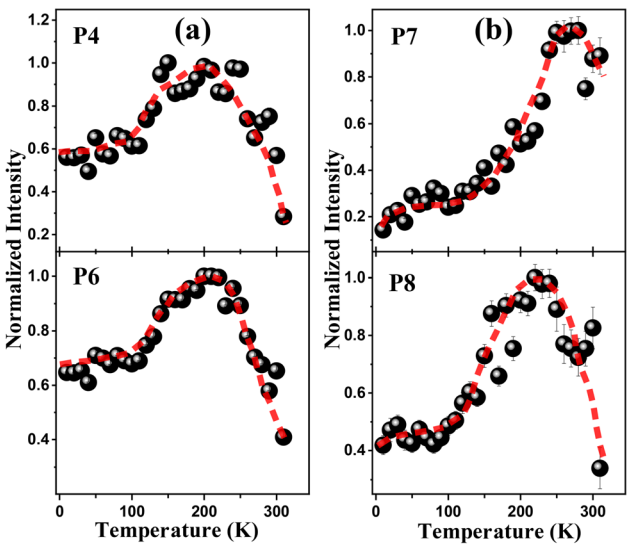

Fig. 4 Temperature dependence of the normalized intensity of the phonon modes P4 and P6 (a), and P7 and P8 (b). The dashed red lines are drawn as a guide for the eye.

further rise in temperature above 200–220 K. Similarly, the intensity of the P7 mode attains a maximum at around ~240–260 K. Such temperature-dependent intensity of the phonon modes suggests the involvement of an intriguing mechanism.

Generally, the temperature-dependent Raman scattering intensity of the phonon modes under non-resonant conditions can be described using the Bose–Einstein function. For the Stokes–Raman scattering case, the intensity of the first-order phonon (first-order Raman scattering), second-order sum of two phonons (creation of two phonons; second-order Raman scattering) and second-order difference of two phonons (creation of one phonon while annihilation of the second phonon; second-order Raman scattering) is given as $(n_1 + 1)$, $(n_1 + 1)(n_2 + 1)$, and $(n_1 + 1)(n_2)$, respectively, where n denotes the Bose–Einstein factor and is given as $n = [\exp(\hbar\omega/\kappa_B T) - 1]^{-1}$.[52] It is worth noting that the Bose–Einstein factor is expected to increase with the increase in temperature and so the intensity of the phonon modes is also expected to increase. Our observation clearly suggests that the Bose–Einstein expression alone is not sufficient to explain the temperature-dependent intensity of the phonon as shown in Fig. 4.

It is worth noting that the quantum mechanical picture has played a crucial role in understanding the temperature-dependent intensity of phonons, especially in the vicinity of the resonance effect, in semiconducting materials.[5,13] Moreover, the excitonic energy states show a strong dependence on the temperature. This indicates that the crossover between non-resonance and resonance conditions can not only be obtained by varying the laser excitation energy but can also be achieved by varying the temperature. The crossover between non-resonance and resonance conditions with varying temperature may result in the modulation in the intensity of the phonon modes. Considering the quantum mechanical picture, the intensity of the phonon for a first-order Raman scattering process is given as:[52,53]

$$I = \left| \sum_{m,n,n'} \frac{\langle m|H_2|n'\rangle\langle n'|H_{\text{el-ph}}|n\rangle\langle n|H_1|m\rangle}{(E_L - \Delta E_{mn})(E_s - \Delta E_{mn'})} \right|^2 \quad (6)$$

where $|m\rangle$, $|n\rangle$, and $|n'\rangle$ represent the ground state and the intermediate states, respectively. H_1 and H_2 are the Hamiltonians representing the electron–photon (absorption) and electron–photon (emission) process, respectively. $H_{\text{el-ph}}$ is the electron–phonon interaction Hamiltonian. $\Delta E_{mn} = (E_n - E_m + i\gamma_1)$ and $\Delta E_{mn'} = (E_{n'} - E_m + i\gamma_2)$ represent the energy difference between the intermediate state E_n and the ground state E_m, and the intermediate state $E_{n'}$ and the ground state E_m, respectively. The terms γ_1 and γ_2 are related to the finite lifetime of the intermediate states $|n\rangle$ and $|n'\rangle$. $E_L = \hbar\omega_L$ and $E_s = \hbar\omega_s = \hbar\omega_L - \hbar\omega_{ph}$ correspond to the incident and scattered photon energy, respectively, and ω_{ph} is the frequency of the phonon involved in the Raman scattering process. For the case when the intermediate states are real, $E_n - E_m$ and $E_{n'} - E_m$ can be written as excitonic energy states (E_x) or band gap (E_g) of the materials. When the laser excitation energy is close to the excitonic energy states (E_x) or band gap (E_g), it gives rise to the resonance effect, which significantly enhances the intensity of the phonon. Changes in laser excitation energy result in a crossover between resonance and resonance conditions. Furthermore, we note that the excitonic energy states (E_x) or

band gap (E_g) is also dependent on the temperature, suggesting that temperature is an additional parameter that could also lead to crossover between resonance and resonance conditions. In the vicinity of the excitonic resonance effect, the numerator term in eqn (6) may become weak as compared to the denominator and the Raman scattering intensity of the phonon mode may be written as:

$$I \propto \left| \frac{1}{\{E_x(T) - E_L + i\gamma_x(T)\}\{E_x(T) - E_s + i\gamma_x(T)\}} \right|^2 \quad (7)$$

where $E_x(T)$ and $\gamma_x(T)$ are the temperature-dependent transition energies and linewidths corresponding to excitonic energy states, respectively. Eqn (7) suggests that the resonance condition could be achieved by changing the incident excitation laser energy as well as by changing the temperature. Generally, with increasing temperature, the energy of the excitonic states decreases. The change in the excitonic energy with temperature results in the crossover between non-resonance and resonance conditions, which may lead to the modulation in intensity of the phonon while keeping the laser excitation energy fixed. We note that SnS_2 is a semiconducting material with a band gap of E_g ~2.3–2.5 eV. We have recorded the Raman spectra with laser excitation energy of 2.33 eV, clearly reflecting that the system is under the resonance effect near room temperature. Hence, the enhancement in the intensity of the phonon modes is due to the resonance observed when increasing the temperature in the range of ~180–240 K. In section 3.5, we investigate and explain the temperature dependence of the PL peaks, which support our results about crossover between non-resonance and resonance conditions for the current system.

3.3. Low-frequency shear mode

In this section, we shed light on the low-frequency interlayer phonon mode P1 observed close to ~27 cm^{-1}. We note that interlayer low-frequency phonons in layered 2D materials appear due to the interlayer interaction between the adjacent layers, and they play an important role in the investigation of a wide range of aspects of materials such as strain effects, interlayer interaction strength, stacking configuration, electron–phonon coupling, and number of layers.[34,39,54–56] To the best of our knowledge, detailed investigations of the low-frequency Raman dynamics of 2H-SnS_2 are still lacking so far. P.H. Tan *et al.*,[57] revealed the Raman dynamics of such asymmetric shear modes in graphene as a function of the layers.

Fig. 5(a) shows the temperature evolution of the low-frequency P1 mode, which appears due to the in-plane (shear) or out-of-plane (breathing) interaction of the adjacent layers. We observed the asymmetrical nature of the P1 mode and surprisingly the asymmetricity survives even up to our highest recorded temperature, as shown in Fig. 1(a) and 5(a). This low-frequency Raman mode provides direct measurement of the interlayer coupling between two adjacent layers in van der Waals materials. The asymmetric nature of the P1 mode may be due to quantum interference between a Raman-allowed phonon and a continuum of Raman-active electronic or multiphoton transitions.[58]

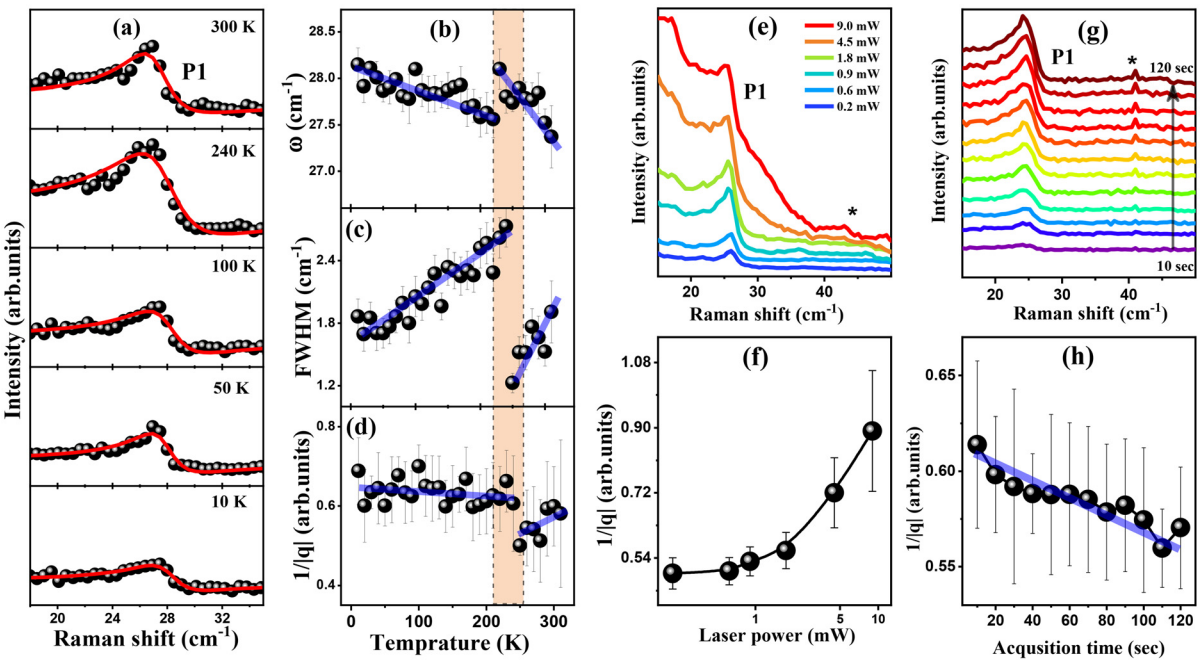

Fig. 5 (a) The temperature variation of the Fano peak (P1). (b) and (c) Temperature dependence of the frequency and FWHM of the Fano peak P1, respectively. (d) Temperature dependence of the coupling strength 1/|*q*|. (e) The laser excitation power dependence of the Raman spectrum in the frequency range of ~15 to 50 cm^{-1} using laser excitation of 532 nm. (f) Laser excitation power dependence of the coupling strength 1/|*q*| at room temperature. (g) The evolution of the Raman spectrum in the frequency range of ~15 to 50 cm^{-1} as a function of spectrum acquisition time at room temperature. (h) The coupling strength 1/|*q*| as a function of the acquisition time. Semi-transparent blue lines are drawn as a guide for the eye.

To investigate the process quantitatively, we analyzed this asymmetric line shape of the P1 mode using a Breit–Wagner–Fano (BWF) function, which is given by:[57,59] $I(\omega) \propto \frac{(1+\delta/q)^2}{1+\delta^2}$, where $\delta = \frac{\omega-\omega_0}{\Gamma}$, and $I(\omega)$ is the Raman intensity as a function of frequency ω. The terms ω_0 and Γ denote the frequency and FWHM of the bare/uncoupled phonon, respectively, while q is the asymmetry parameter that characterizes the coupling strength between the phonon and the continuum, quantified by the parameter $1/|q|$. In the limit $1/|q| \to \infty$, coupling is stronger and causes the peak to become more asymmetric while in the limit $1/|q| \to 0$, coupling is weak and this results in the Lorentzian line shape.[29,60] The solid red lines in Fig. 5(a) are the best fit using the BWF function. Fig. 5(b) and (c) show the temperature dependence of the frequency and linewidth of peak P1 in the temperature range of ~10–310 K. For mode P1, both parameters (*i.e.*, frequency and linewidth) show discontinuity in the temperature range of ~220–250 K and this discontinuity may be due to the resonance phenomena in this temperature range. Fig. 5(d) shows the temperature dependence of the coupling strength ($1/|q|$) in the temperature range of 10–310 K. We note that with decreasing temperature $1/|q|$ increases slightly, indicating weak dependence on the temperature and showing discontinuity in the temperature range of ~220–250 K.

The Fano asymmetry may be influenced by laser power, due primarily to the generation of photoexcited charge carriers, which increase the free electron plasma density as laser power rises.[61,62] We also conducted Raman measurements in the low-frequency region under varying laser excitation powers and acquisition times (spectrum collection times) to investigate their effect on the Fano interaction. Fig. 5(e) and (f) show the evolution of the Fano peak P1 and the coupling strength ($1/|q|$) as a function of the laser power. The coupling strength increases exponentially with increasing laser power, indicating that the coupling between phonon and continuum increases with laser power. This enhancement in the coupling may have occurred due to the laser-induced electron plasma. Fig. 5(g) shows the evolution of peak P1 as a function of acquisition time, *i.e.*, recording time of the spectrum from 10 s to 120 s increasing at 10 s intervals. Fig. 5(h) shows the coupling strength ($1/|q|$) dependence on the acquisition time of the spectrum. With increasing acquisition time, $1/|q|$ decreases linearly, although the change is small. This suggests there is no significant plasma induced with increasing spectrum acquisition time. In contrast, increasing the laser excitation power induces more electron–hole plasma, thus resulting in an increase in the coupling strength. This observation suggests that we can control the coupling between the phonon and the underlying continuum and/or multiphoton transitions with laser excitation power.

3.4. Polarization dependence of the phonon modes

To investigate the polarization dependence of the Raman spectrum of VA 2H-SnS_2, we performed polarization-dependent Raman measurements at room temperature by rotating the polarization of the incident light while keeping the polarization of the scattered light fixed. Ding *et al.*[9] performed a polarization-dependent study on SnS_2 by rotating the sample and suggesting applications of this material in the field of polarizing devices. VA semiconducting materials are potential candidates for applications in optoelectronic and other devices. Hence, it is important to study the polarization dependence of phonons in the current system.

Fig. 6(a) shows the polar plot for the intensity of the phonon modes P2–P4, P6, P7, and P8 at a temperature of 300 K. P2 and P3 are weak peaks and P7 and P8 are second-order phonon peaks. P4 is a weak peak with E_g symmetry, and it is doubly degenerate while P6 is the most prominent peak with A_g symmetry. The Raman tensors for the phonon modes with symmetries E_g and A_g are listed in the ESI.†[15] To investigate the polarization dependence of the phonon modes P4 and P6, we used the semi-classical approach and according to this, the intensity of the phonon modes is given as $I \propto |\hat{e}_s^T \cdot R \cdot \hat{e}_i|^2$, where T is the transpose, $\hat{e}_i$ and $\hat{e}_s$ are the unit vectors in the direction of the incident and scattered light electric field, respectively, and R is the Raman tensor for Raman modes. The unit vectors in the direction of the incident and scattered light can be written in matrix form as $\hat{e}_i = [\cos(\theta + \theta_0)\ \sin(\theta + \theta_0)\ 0]$ and $\hat{e}_s = [\cos(\theta_0)\ \sin(\theta_0)\ 0]$, respectively, where θ is the angle between unit vectors of incident and scattered light and θ_0 is the arbitrary angle between the polarization of the scattered light and the x-axis as shown in the schematic in Fig. 6(c). The intensity of the phonon with E_g and A_g symmetries depends on the polarizing angle (θ) and associated Raman tensors and is given as:

$$I_{E_g} = |c\cos(\theta)(\cos^2(\theta_0) - \sin^2(\theta_0)) - c\sin(2\theta_0)\sin(\theta)|^2, \quad (8a)$$

$$I_{E_g} = |c\sin(\theta)(\sin^2(\theta_0) - \cos^2(\theta_0)) - c\sin(2\theta_0)\cos(\theta)|^2 \quad (8b)$$

$$I_{A_g} = a^2\cos^2(\theta) \quad (9)$$

Without loss of generality, we consider $\theta_0 = 0$. This makes the above eqn (8(a)) and (8(b)) become:

$$I_{E_g} = c^2\cos^2(\theta), \quad (10a)$$

$$I_{E_g} = c^2\sin^2(\theta) \quad (10b)$$

In Fig. 6(a), the solid red line shows the fitted curve, by adding eqn (10(a)) and (10(b)),

$$I_{E_{1g}} = c^2\cos^2(\theta) + c^2\sin^2(\theta) = c^2 \quad (11)$$

The polar plot for the intensity of the phonon mode P6 with A_g symmetry shows nearly circular symmetry, while according to eqn (9), it should be a two-fold kind of symmetry. Ding *et al.*[9] performed polarization-dependent Raman measurements on SnS_2 crystals in basal and cross-plane configurations and observed circular and two-fold symmetry for basal and cross-planes, respectively, for the A_g (~314 cm^{-1}) mode. In our measurement, we observed circular symmetry

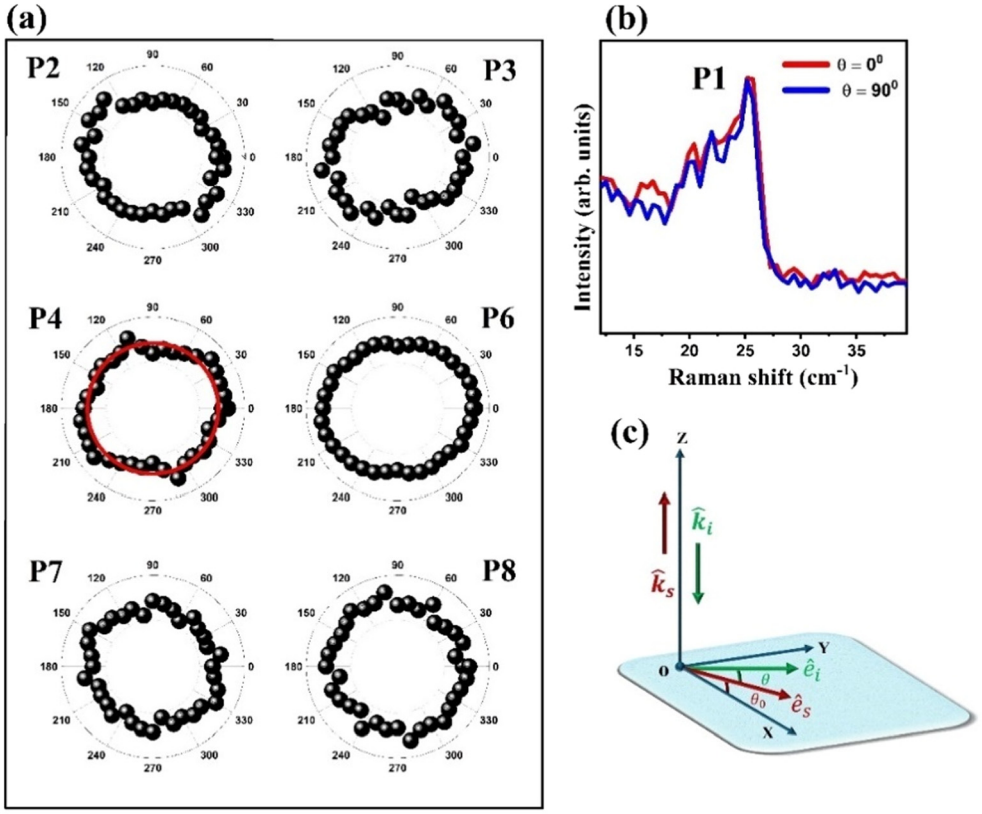

Fig. 6 (a) The intensity polar plot for VA SnS_2 using 532 nm (2.33 eV) laser excitation for peaks P2–P4, and P6–P8 at 300 K. (b) Polarization dependance of the low frequency interlayer mode P1. (c) The schematic of the polarization configuration.

for the P6 (A_{1g}) mode and this may be due to the vertically aligned SnS_2 grown by the CVD method. M. Hulman *et al.*,[63] also studied polarization-dependent Raman measurements of vertically and horizontally aligned MoS_2 and observed different polarization dependencies for the mode with E_g symmetry.

Fig. 6(b) shows the polarization dependence of the low-frequency interlayer mode P1. It shows independence from the polarizing angle (θ). This suggests that mode P1 is the low-frequency interlayer shear mode, which is caused by the in-plane vibrations of the adjacent layers. By rotating the electric field of the incoming light, our polarization analysis demonstrates the polarization dependence of the phonon modes, primarily the low-frequency mode P1 and the high-frequency modes P4 and P6 in VA SnS_2.

3.5. Temperature- and laser power-dependence of photoluminescence

To investigate the dynamics of excitonic quasiparticles, temperature-dependent PL spectroscopy has been widely used.[64–70] To acquire knowledge about the nature of excitonic quasiparticles in 2D materials, laser excitation power-dependent PL measurements have also been reported for other 2D materials.[71] In 2D semiconducting materials, the coupling of excitonic quasiparticles (excitons, trions, and bi-excitons) with phonons and charge carriers plays an important role in controlling optical properties. Burton *et al.*,[72] studied the optical and electronic properties of single-crystal SnS_2. To the best of our knowledge, no detailed temperature-dependent PL spectroscopy study has been reported for CVD-grown VA 2H-SnS_2 of few-layered thickness. Hence, we performed and analyzed both temperature- and power-dependent PL measurements on VA 2H-SnS_2. Fig. 7(a) shows the evolution of the fitted PL spectra at four different temperatures of 5, 150, 230, and 300 K (for detailed temperature evolution of the PL spectra, see Fig. S2†). PL spectra were fitted with the sum of the Voigt function to extract the peak position, FWHM and intensity of the individual PL peaks at each measurement of the recorded temperature- and power-dependent PL spectra. The Voigt function is the spectral convolution of the Lorentzian and Gaussian functions and is given as:[73,74]

$$y = y_0 + A\frac{2\ln 2}{\pi^{3/2}}\frac{\Gamma_L}{\Gamma_G}\int_{-\infty}^{\infty}\frac{e^{-t^2}}{\left(\sqrt{\ln 2}\frac{\Gamma_L}{\Gamma_G}\right)^2+\left(\sqrt{4\ln 2}\frac{x-x_{c_1}}{\Gamma_G}-t\right)^2}dt \quad (12)$$

where x_{c_1} and A are the center and area of the Voigt function. Γ_L and Γ_G are the Lorentzian and Gaussian linewidths.

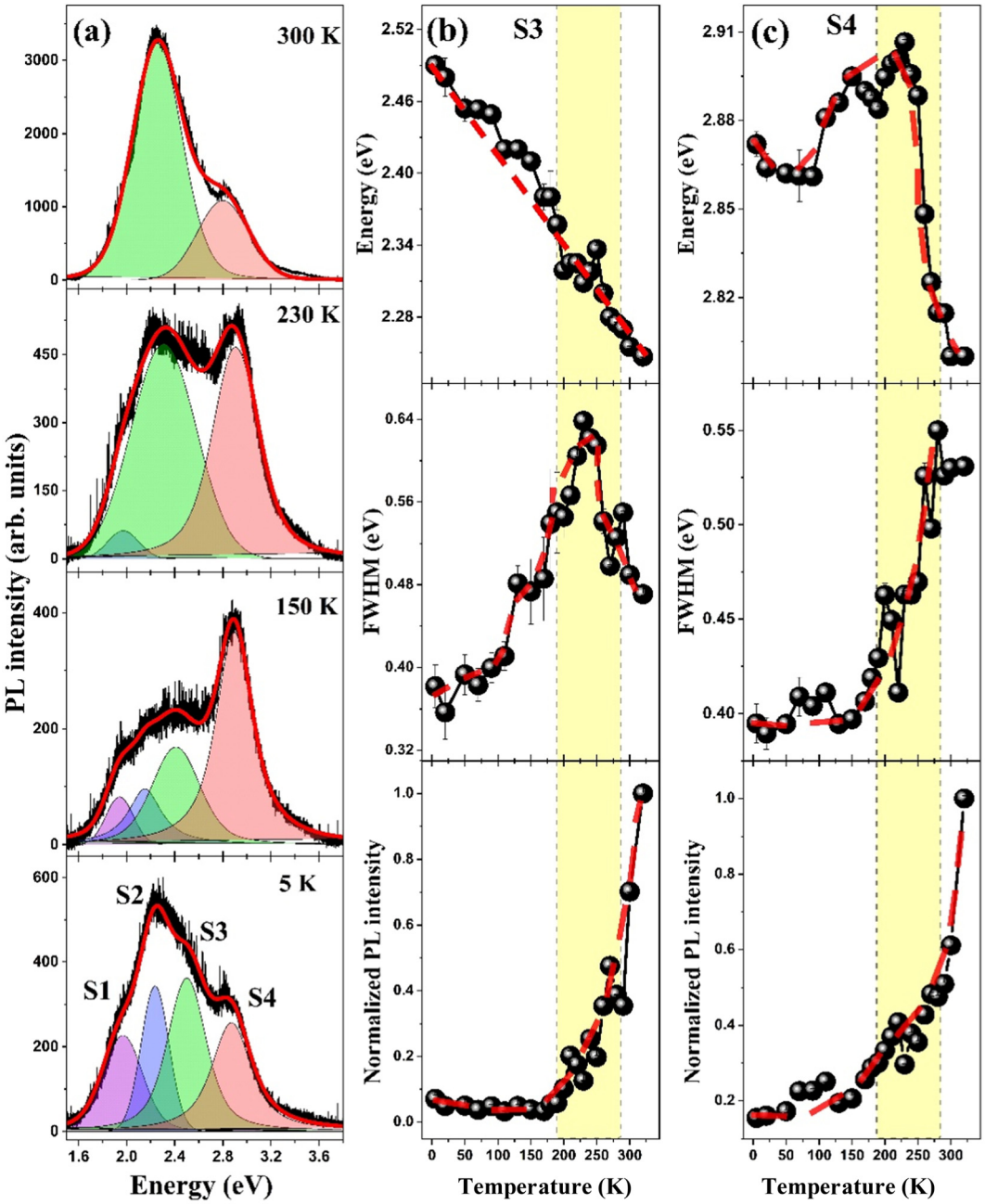

Fig. 7 (a) The evolution of the PL spectra. (b) and (c) The temperature dependence of the peak position, FWHM and intensity of PL peaks S3 and S4, respectively. Dashed red lines are drawn as a guide for the eye.

At low temperatures, we fitted PL spectra with four individual peaks, namely S1–S4. As we increase the temperature, peaks S1 and S2 become weak and vanish after a certain temperature. Peaks S3 and S4 show a strong temperature dependence in the temperature range of ~5–320 K. Fig. 7(b) and (c) show the temperature dependence of the extracted parameters in the temperature range of ~5–320 K. For peak S3, the peak position gradually decreases with increasing temperature, while FWHM increases gradually up to ~230 K and decreases with further increases in temperature. The position of peak S3 approaches an energy of ~2.33 eV in the temperature range of ~200–260 K, which is the energy of the 532 nm (2.33 eV) laser excitation we used for the temperature-dependent Raman measurement. This suggests a strong enhancement in the resonant Raman scattering in this temperature range. For peak S4, the peak position decreases slightly with an increase in temperature up to ~90 K. With a further increase in temperature, the peak position increases up to ~230 K and then decreases drastically with a further increase in temperature. The FWHM of peak S4 increases slightly with increasing temp-

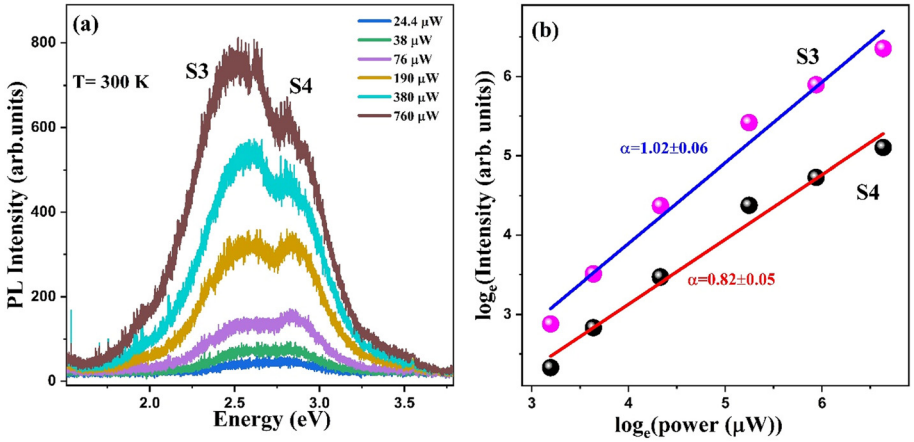

Fig. 8 (a) The evolution of PL spectra as a function of 325 nm (3.81 eV) laser excitation power at room temperature. (b) Shows the PL intensity of the peaks S3 and S4 as a function of laser excitation (graph plotted on the $\log_e$–$\log_e$ scale). The solid lines are the fitted curves derived from the power law, $I \propto P^{\alpha}$.

erature up to ~170 K and increases drastically with a further increase in temperature. The PL intensity of both peaks S3 and S4 slightly increases with an increase in temperature until ~180 K and increases exponentially with a further increase in the temperature. Such an increase in the intensity of the PL peak with increasing temperature is also observed for few-layered $MoSe_2$.[65] To investigate the nature of the PL peaks, we also performed power-dependent PL measurements at room temperature. Fig. 8(a) shows the evolution of the PL spectra as a function of laser power, and mainly displays the peaks S3 and S4. Fig. 8(b) shows the integrated PL intensity of the peaks S3 and S4 as a function of the laser power. With increasing laser power, the intensity of both peaks increases and shows a strong dependence. We fitted the intensities with a power law: $I \propto P^{\alpha}$. The extracted values of the exponent α for peaks S3 and S4 are 1.02 ± 0.06 and 0.82 ± 0.05, respectively. These values of α suggest the excitonic nature of both peaks S3 and S4.[75] D. Y. Lin *et al.*[76] performed temperature-dependent piezo-reflectance measurements on layered ternary $SnS_{2-x}Se_x$ and also observed similar behavior for the excitonic peaks at around ~2.3 eV.

4. Conclusion

In conclusion, we performed detailed inelastic light (Raman) scattering and photoluminescence measurements and analysis on vertically aligned 2D 2H-SnS_2 grown by the CVD method. Our temperature-dependent Raman measurements reveal temperature-dependent phonon–phonon interactions, thermal expansion coefficients and intensities of the observed phonon modes. We also performed polarization measurements to investigate the symmetry of the phonon modes. Our temperature- and laser power-dependent PL measurements provide interesting results about the dynamics of the observed excitonic peaks. Our results suggest tunability (crossover) between resonant and non-resonant Raman scattering with changes in temperature for 2H-SnS_2 and our detailed investigation provides crucial understanding that may help in the design and fabrication of future optoelectronic devices based on VA semiconducting SnS_2 and other such materials.

Conflicts of interest

There are no conficts to declare.

Data availability

All data that support the findings of this study are included within the article and the ESI.†

Acknowledgements

P. K. thanks SERB (Project No. CRG/2023/002069) for financial support and IIT Mandi for the experimental facilities.

References

1 J. Cao, Q. Chen, X. Wang, Q. Zhang, H.-D. Yu, X. Huang and W. Huang, Recent development of gas Sensing platforms based on 2D atomic crystals, *Research*, 2021, **10**, 34133.
2 C. Xie, C. Mak, X. Tao and F. Yan, Photodetectors based on two–dimensional layered materials beyond graphene, *Adv. Funct. Mater.*, 2017, **27**, 1603886.
3 Q. H. Wang, K. Kalantar-Zadeh, A. Kis, J. N. Coleman and M. S. Strano, Electronics and optoelectronics of two-dimensional transition metal dichalcogenides, *Nat. Nanotechnol.*, 2012, **7**, 699.

4 Y. Huang, *et al.*, Tin disulfide an emerging layered metal dichalcogenide semiconductor: materials properties and device charactrization, *ACS Nano*, 2014, **10**, 10743.
5 H. Zobeiri, S. Xu, Y. Yue, Q. Zhang, Y. Xie and X. Wang, Effect of temperature on Raman intensity of nm-thick WS_2: combined effects of resonance Raman, optical properties, and interface optical Interference, *Nanoscale*, 2020, **12**, 6064.
6 J. B. Liu, J. Y. Hu, C. Liu, Y. M. Tan, X. Peng and Y. Zhang, Mechanically exfoliated MoS_2 nanosheets decorated with SnS_2 nanoparticles for high-stability gas sensors at room temperature, *Rare Met.*, 2022, **40**, 1536.
7 H. Xiao, Y. C. Zhang and H. X. Bai, Molten salt synthesis of SnS_2 microplate particles, *Mater. Lett.*, 2009, **63**, 809.
8 L. Xu, P. Zhang, *et al.*, Large-scale growth and field-effect transistors electrical engineering of atomic–layer SnS_2, *Small*, 2019, **15**, 1904116.
9 Y. Ding, W. Zheng, X. Lu, Y. Liang, Y. Zhu, M. Jin and F. Huang, Raman tensor of layered SnS_2, *J. Phys. Chem. Lett.*, 2020, **11**, 10094.
10 M. R. Molas, K. Nogajewski, M. Potemski and A. Babiński, Raman scattering excitation spectroscopy of monolayer WS_2, *Sci. Rep.*, 2017, **7**, 5036.
11 N. B. Shinde, *et al.*, Davydov splitting, double-resonance Raman scattering, and disorder-induced second-order rrocesse sin chemical vapor deposited MoS_2 thin films, *J. Phys. Chem. Lett.*, 2021, **12**, 6197.
12 M. Bhatnagar, T. Wozniak, *et al.*, Temperature induced modulation of resonant Raman scattering in bilayer 2H-MoS_2, *Sci. Rep.*, 2022, **12**, 14169.
13 J. H. Fan, P. Gao, A. M. Zhang, B. R. Zhu, H. L. Zeng, X. D. Cui, R. He and Q. M. Zhang, Resonance Raman scattering in bulk 2H-MX_2 (M = Mo, W; X = S, Se) and monolayer MoS_2, *J. Appl. Phys.*, 2014, **115**, 053527.
14 K. Golasa, *et al.*, Multiphonon resoanat Raman scattering in MoS_2, Appl, *Phys. Lett.*, 2014, **104**, 092106.
15 T. Sriv, K. Kim and H. Cheong, Low-frequency Raman spectroscopy of few-layer 2H-SnS_2, *Sci. Rep.*, 2018, **8**, 10194.
16 K. X. Chen, X. M. Wang, D. C. Mo and S. S. Lyu, Thermoelectric properties of transition metal dichalcogenides: from monolayers to nanotubes, *J. Phys. Chem. C*, 2015, **119**, 26706.
17 G. Zhang and Y. W. Zhang, Thermoelectric properties of two-dimensional transition metal dichalcogenides, *J. Mater. Chem. C*, 2017, **5**, 7684.
18 P. Soubelet, A. E. Bruchhausen, A. Fainstein, K. Nogajewski and C. Faugeras, Resonance effects in the Raman scattering of monolayer and few-layer $MoSe_2$, *Phys. Rev. B*, 2016, **93**, 155407.
19 X. Cong, X. L. Liu, M. L. Lin and P. H. Tan, Application of Raman spectroscopy to probe fundamental properties of two-dimensional materials, *npj 2D Mater. Appl.*, 2020, **4**, 13.
20 G. P. Srivastava and I. O. Thomas, Temperature-dependent Raman linewidths in transition-metal dichalcogenides, *Phys. Rev. B*, 2018, **98**, 035430.
21 D. Kumar, B. Singh, R. Kumar, M. Kumar and P. Kumar, Davydov splitting, resonance effect and phonon dynamics in chemical vapor deposition grown layered MoS_2, *Nanotechnology*, 2021, **32**, 285705.
22 T. Jena, M. T. Hossain and P. K. Giri, Temperature-dependent Raman study and determination of anisotropy ratio and in-plane thermal conductivity of low-temperature CVD-grown $PdSe_2$ using unpolarized laser excitation, *J. Mater. Chem. C*, 2021, **9**, 16693.
23 Y. Lv, L. Cao, X. Li, B. Zhang, K. Wang, B. Pang and L. Ma, Composition and temperature-dependent phase transition in miscible $Mo_{1-x}W_xTe$ single crystals, *Sci. Rep.*, 2017, **7**, 44587.
24 D. Kumar, V. Kumar, R. Kumar, M. Kumar and P. Kumar, Electron-phonon coupling, thermal expansion coefficient, eesonance effect, and phonon dynamics in high-quality CVD-grown monolayer and bilayer $MoSe_2$, *Phys. Rev. B*, 2022, **105**, 085419.
25 J. B. Wu, X. Zhang, M. Ijäs, W. P. Han, X. F. Qiao, X. L. Li, D. S. Jiang, A. C. Ferrari and P. H. Tan, Resonant Raman spectroscopy of twisted multilayer graphene, *Nat. Commun.*, 2014, **5**, 5309.
26 X. Huang, Y. Gao, T. Yang, W. Ren, H. M. Cheng and T. Lai, Quantitative analysis of temperature dependence of Raman shift of monolayer WS_2, *Sci. Rep.*, 2016, **6**, 32236.
27 J. Park, Y. Kim, Y. I. Jhon and Y. M. Jhon, Temperature dependent Raman spectroscopic study of mono-, bi-, and tri-layer molybdenum ditelluride, *Appl. Phys. Lett.*, 2015, **107**, 153106.
28 S. Sinha, V. Sathe and S. K. Arora, Temperature dependent Raman investigations of few-layered WS_2 nanosheets, *Solid State Commun.*, 2019, **298**, 113626.
29 A. G. Chakkar, D. Kumar and P. Kumar, Broken weak and strong spin rotational symmetries and tunable interactions between phonons and the continuum in $Cr_2Ge_2Te_6$, *Phys. Rev. B*, 2024, **109**, 134406.
30 M. A. Susner, R. Rao, A. T. Pelton, M. V. McLeod and B. Maruyama, Temperature-dependent Raman scattering and X-ray diffraction study of phase transitions in layered multiferroic $CuCrP_2S_6$, *Phys. Rev. Mater*, 2020, **4**, 104003.
31 B. Huang, J. Cenker, *et al.*, Tuning inelastic light scattering via symmetry control in the two dimensional magnet CrI_3, *Nat. Nanotechnol.*, 2020, **15**, 212.
32 Y. Choi, S. Lee, J. H. Lee, S. Lee, M. J. Seong and K. Y. Choi, Bosonic Spinons in Anisotropic Triangular Antiferromagnets, *Nat. Commun.*, 2021, **12**, 1.
33 L. J. Sandilands, Y. Tian, K. W. Plumb, Y. J. Kim and K. S. Burch, Scattering continuum and possible fractionalized excitations in α-$RuCl_3$, *Phys. Rev. Lett.*, 2015, **114**, 147201.
34 M. Bayle, *et al.*, Determining the number of layers in few-layer graphene by combining Raman spectroscopy and optical contrast, *J. Raman Spectrosc.*, 2018, **49**, 36.
35 N. Khan, D. Kumar, S. Semwal, *et al.*, Short and long-range magnetic ordering and emergent topological transition in $(Mn_{1-x}Ni_x)_2P_2S_6$, *Sci. Rep.*, 2025, **15**, 4438.

36 Y. Tian, M. J. Gray, H. Ji, R. J. Cava and K. S. Burch, Magneto-elastic coupling in a potential ferromagnetic 2D atomic crystal, *2D Mater.*, 2016, **3**, 025035.
37 J. Kim, J. Lee and H. Cheong, Polarized Raman spectroscopy for studying two dimensional materilas, *J. Phys.: Condens. Matter*, 2020, **32**, 343001.
38 H. Sahin, S. Tongay, S. Horzum, W. Fan, J. Zhou, J. Li, J. Wu and F. M. Peeters, Anomalous Raman spectra and thickness-dependent electronic properties of WSe_2, *Phys. Rev. B: Condens. Matter Mater. Phys.*, 2013, **87**, 165409.
39 L. Liang, J. Zhang, B. G. Sumpter, Q. H. Tan, P. H. Tan and V. Meunier, Low-frequency shear and layer-breathing modes in Raman scattering of two-dimensional materials, *ACS Nano*, 2017, **11**, 11777.
40 Y. Choi, S. Lee, J. H. Lee, S. Lee, M. J. Seong and K. Y. Choi, Bosonic spinons in anisotropic triangular antiferromagnets, *Nat. Commun.*, 2021, **12**, 6453.
41 A. Kumar, N. Sharma, A. P. Gutal, D. Kumar, P. Kumar, M. Paranjothy and M. Kumar, Growth and NO_2 gas sensing mechanisms of vertically aligned 2D SnS_2 flakes by CVD: experimental and DFT studies, *Sens. Actuators, B*, 2022, **353**, 131078.
42 A. Kumar, A. P. Gutal, N. Sharma, D. Kumar, G. Zhang, H. Kim, P. Kumar, M. Paranjothy, M. Kumar and M. S. Strano, Investigations of vacancy-assisted selective detection of NO_2 molecules in vertically aligned SnS_2, *ACS Sens.*, 2023, **8**, 1357.
43 C. Julien, H. S. Mavi, K. P. Jain and M. Balkanski, Resonant Raman scattering studies of SnS crystal, *Mater. Sci. Eng. B*, 1994, **23**, 98–104.
44 D. G. Mead and J. C. Irwin, Raman spectra of SnS_2 and $SnSe_2$, *Solid State Commun.*, 1976, **20**, 885.
45 J. M. Skelthon, *et al.*, Lattice dynamics of the SnS_2, SnS, Sn_2S_3: vibrational spectra and thermal transport, *Phys. Chem. Chem. Phys.*, 2017, **19**, 14452.
46 B. Singh, S. Kumar and P. Kumar, Broken translational and rotational symmetries in $LiMn_{1.5}Ni_{0.5}O_4$ spinel, *J. Phys.: Condens. Matter*, 2019, **31**, 395701.
47 D. Kumar, B. Singh, P. Kumar, V. Balakrishnan and P. Kumar, Thermal expansion coefficient and phonon dynamics in coexisting allotropes of monolayer WS_2 probed by Raman scattering, *J. Phys.: Condens. Matter*, 2019, **31**, 505403.
48 M. Balkanski, R. F. Wallis and E. Haro, Anharmonic effects in light scattering due to optical phonons in silicon, *Phys. Rev. B: Condens. Matter Mater. Phys.*, 1983, **28**, 1928.
49 O. Abdul-Aziz, D. Wolverson, C. J. Sayers, E. Carpene, F. Parmigiani, H. Hedayat and P. H. M. van Loosdrecht, Resonance-induced anomalies in temperature-dependent Raman scattering of $PdSe_2$, *J. Mater. Chem. C*, 2024, **12**, 11402.
50 M. Bhatnagar, T. Wozniak, *et al.*, Temperature induced modulation of resonant Raman scattering in bilayer 2H-MoS_2, *Sci. Rep.*, 2022, **12**, 14169.
51 R. N. Gontijo, T. Zhang, K. Fujisawa, A. L. Elías, M. A. Pimenta, A. Righi, M. Terrones and C. Fantini, Multiple excitations and temperature study of the disorder-induced Raman bands in MoS_2, *2D Mater.*, 2021, **8**, 035042.
52 M. Cardona and G. Guntherodt, *Light scattering in solids II*, Springer-Verlag, Berlin, 1982.
53 P. Y. Yu and M. Cardona, *Fundamentals of semiconductor*, Springer- Verlag, Berlin, 2010.
54 N. Van Velson, H. Zobeiri and X. Wang, Thickness-dependent Raman scattering from thin-film systems, *J. Phys. Chem. C*, 2023, **127**, 2995.
55 M. Kim, S. Han, J. H. Kim, J. U. Lee, Z. Lee and H. Cheong, Determination of the thickness and orientation of few-layer tungsten ditelluride using polarized Raman spectroscopy, *2D Mater.*, 2016, **3**, 034004.
56 X. Zhang, X. F. Qiao, W. Shi, J. Bin Wu, D. S. Jiang and P. H. Tan, Phonon and Raman scattering of two-dimensional transition metal dichalcogenides from monolayer, multilayer to bulk material, *Chem. Soc. Rev.*, 2015, **44**, 2757.
57 P. H. Tan, *et al.*, The shear mode of multilayer graphene, *Nat. Mater.*, 2012, **11**, 294.
58 M. V. Klien, *Light scattering in solids, Topics in applied physics*, ed. M. Cardona, Springer, 2nd edn, 1975, vol. 8.
59 U. Fano, Effects of configuration interaction on intensities and phase shifts, *Phys. Rev.*, 1961, **124**, 1866.
60 B. Singh, M. Vogl, S. Wurmehl, S. Aswartham, B. Büchner and P. Kumar, Kitaev magnetism and fractionalized excitations in double perovskite Sm_2ZnIrO_6, *Phys. Rev. Res.*, 2020, **2**, 13040.
61 S. Bhattacharjee and K. K. Chattopadhyay, Laser-induced Fano asymmetry, electron-phonon coupling, and phase transition in lanthanide sesquioxide (Ln_2O_3; Ln = Eu, Gd, Dy) nanoparticles: a Raman spectroscopic investigation, *J. Appl. Phys.*, 2022, **132**, 215107.
62 A. Sunny, A. Thirumurugan and K. Balasubramanian, Laser induced Fano scattering, electron-phonon coupling, bond length and phonon lifetime changes in α-Fe_2O_3 nanostructures, *Phys. Chem. Chem. Phys.*, 2020, **22**, 2001.
63 M. Hulman, M. Sojkova, *et al.*, Polarized raman reveals alignment of few-layer MoS_2 films, *J. Phys. Chem. C*, 2019, **123**, 29468.
64 D. Kumar, R. Kumar, M. Kumar and P. Kumar, Coupled excitonic quasiparticle-electron-phonon and interlayer coupling in vertically and horizontally aligned MoS_2, *J. Mater. Chem. C*, 2022, **10**, 5684.
65 S. Tongay, J. Zhou, C. Ataca, K. Lo, T. S. Matthews, J. Li, J. C. Grossman and J. Wu, Thermally driven crossover from indirect toward direct bandgap in 2D semiconductors: $MoSe_2$ versus MoS_2, *Nano Lett.*, 2012, **12**, 5576.
66 Y. Chen, W. Wen, Y. Zhu, N. Mao, Q. Feng, M. Zhang, H. P. Hsu, J. Zhang, Y. S. Huang and L. Xie, Temperature-dependent photoluminescence emission and Raman scattering from $Mo_{1-x}W_xS_2$ monolayers, *Nanotechnology*, 2016, **27**, 445705.
67 M. D. Tran, J. H. Kim and Y. H. Lee, Tailoring photoluminescence of monolayer transition metal dichalcogenides, *Curr. Appl. Phys.*, 2016, **16**, 1159.

68 W. Zheng, Y. Jiang, X. Hu, H. Li, Z. Zeng, X. Wang and A. Pan, Light emission properties of 2D transition metal dichalcogenides: fundamentals and applications, *Adv. Opt. Mater.*, 2018, **6**, 1800420.

69 J. W. Christopher, B. B. Goldberg and A. K. Swan, Long tailed trions in monolayer MoS_2: temperature dependent asymmetry and resulting red-shift of trion photoluminescence spectra, *Sci. Rep.*, 2017, **7**, 14062.

70 Y. Zgang, *et al.*, On valence-band splitting in layered MoS_2, *ACS Nano*, 2015, **8**, 8514–8519.

71 Y. You, X. Zhang, *et al.*, Observation of biexcitons in monolayer WSe_2, *Nat. Phys.*, 2015, **11**, 477.

72 L. A. Burton, *et al.*, Electronic and optical properties of single crystal of SnS_2, an earth- abundant disulfide photocatalyst, *J. Mater. Chem. A*, 2016, **4**, 1312.

73 M. Marceddu, M. Manca, P. C. Ricci and A. Anedda, The temperature dependence of Cr^{3+}:YAG zero-phonon lines, *J. Phys.: Condens. Matter*, 2012, **24**, 135401.

74 P. C. Ricci, A. Casu and A. Anedda, Effect of the electron-phonon interaction on the luminescence properties of iron ions in YAG crystal, *J. Phys. Chem. A*, 2009, **113**, 13901.

75 M. Tebyetekerwa, J. Zhang, Z. Xu, T. N. Truong, Z. Yin, Y. Lu, S. Ramakrishna, D. Macdonald and H. T. Nguyen, Mechanisms and applications of steady-state photoluminescence spectroscopy in two-dimensional transition-metal dichalcogenides, *ACS Nano*, 2020, **14**, 14579.

76 D. Y. Lin, H. P. Hsu, *et al.*, Temperature dependent excitonic transition energy and enhanced electron-phonon coupling in layered ternary $SnS_{2-X}Se_x$ semiconductor with fully tunable stoichiometry, *Molecules*, 2021, **26**, 2184.